

**Manufacturing Improvement and Thermal Property Characterization of the
Frame Structure of an Ultra-high Throughput Mutational Spectrometer**

by

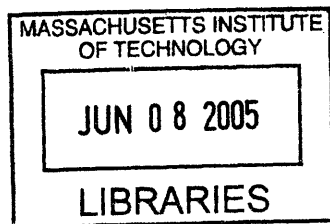
Jiengju J. Lin

SUBMITTED TO THE DEPARTMENT OF MECHANICAL ENGINEERING IN
PARTIAL FULFILLMENT OF THE REQUIREMENTS FOR THE DEGREE OF

BACHELOR OF SCIENCE IN MECHANICAL ENGINEERING
AT THE
MASSACHUSETTS INSTITUTE OF TECHNOLOGY

JUNE 2005

© 2005 Massachusetts Institute of Technology
All rights reserved



ARCHIVES

Signature of Author _____

Department of Mechanical Engineering
May 9, 2005

Certified by _____

Ian W. Hunter
Hatsopoulos Professor of Mechanical Engineering and Professor of Bioengineering
Thesis Supervisor

Accepted by _____

Ernest G. Cravalho
Chairman of the Undergraduate Thesis Committee, Mechanical Engineering

Manufacturing Improvement and Thermal Property Characterization of the Frame Structure of an Ultra-high Throughput Mutational Spectrometer

by

Jiengju J. Lin

Submitted to the Department of Mechanical Engineering
On May 9, 2005 in partial fulfillment of the
Requirements of the Degree of Bachelor of Science in
Mechanical Engineering

ABSTRACT

Constant denaturant capillary electrophoresis (CDCE) is a DNA separation technique that allows the detection of mutants at a fraction of 10^{-6} . CDCE uses a region of constant temperature and constant denaturant concentration to separate fragments with distinct melting points. The concept of the Ultra-high Throughput Mutational Spectrometer (UTMS) will perform massively parallel CDCE on a 100 by 100 capillary array. A modular aluminum structure was designed for the instrument to provide a chamber to house the array and modulate the flow of coolant, providing temperature control. The first iteration of the structure experienced leakage problems, which this project rectified. The structure was also modified to interface with a gel loading mechanism below, and the LED fluorescent excitation array above. The current subunit will enable the testing the complete UTMS system. In addition, an immersion heater was installed in the water-tight structure to simulate the 200 to 275 W heat dissipation within the chamber, caused by Joule heating in the capillary array. Correlation of a theoretical model to experimental data characterized and verified the transient thermal response of the system.

Thesis Supervisor: Ian W. Hunter
Title: Hatsopoulos Professor of Mechanical Engineering

Acknowledgements

I would like to thank Professor Ian Hunter for providing me the opportunity to work in the Bioinstrumentation Lab, and for his guidance and support on this project. The lab has been an incredible resource and intellectually stimulating environment. I am very appreciative of all the members of the Bioinstrumentation Lab, who have been willing and available to familiarizing me with the facility and answering questions.

In particular, I would also like to thank Craig Forest, Michael Del Zio, Tim Suen, and Bryan Woodruff for all their help in this project. Finally, I would like thank Fred Cote of the Edgerton Center and Steve Haberek of the Pappalardo lab for their consultation and advice with fabrication.

Table of Contents

2.0 Genetic Variation	11
2.1 Genetic Analysis	12
2.2 Mutational Spectrometry	14
3.0 Instrument Concept	14
3.1 Design Requirement for Experimental Simulation	17
4.0 Modifications of the Modular Structure	19
4.1 End Plate Designs	20
4.2 Simulated Power Input	22
4.3 Interface with Capillary Array/Gel Loader Assembly	23
4.4 Capillary Array Upper Mount	24
5.0 Manufacturing of Subunit	25
5.1 Modular Frame	25
5.2 Flat Gaskets	26
5.3 Small Diameter O-Ring Glands	27
5.4 Assembly of Subunit	27
6.0 Theory	28
6.1 Thermal Resistance Model	29
6.2 Convection Heat Transfer Through Water	31
6.4 Deriving the Transient Model	33
7.0 Simulated Testing of the Thermal Response	36
7.1 Procedure	38
8.0 Results	39
9.0 Conclusion and Outlook	43
References	47
Appendix A: Determination of h_c for Recirculating Water	49
Appendix B: Nusselt Number Arrangement Factor	50
Appendix C: Thermal Resistance Calculations for the Subunit Thermal Circuit	51

Table of Figures

Figure 1. Schematic of ultra high throughput mutational spectrometer	16
Figure 2. Polyamide coated quartz capillary.....	17
Figure 3. Capillary clamp plate.....	19
Figure 4. Top plate with square pocket flange adaptor and O-ring gland.	20
Figure 5. Bottom plate with flange adaptor and 6 mm key slots for mounting supports.	21
Figure 6. mk Series 25 angle CAD model and mk angle installed in UTMS base.....	21
Figure 7. Omega RI Series screw plug type immersion heater.....	22
Figure 8. Upper mount plate.	24
Figure 9. Rubber-bonded paper gasket.....	26
Figure 10. Cross bolt tightening pattern	28
Figure 11. Schematic diagram of thermal resistances	29
Figure 12. Control volume of frame used for theoretical model	31
Figure 13. Schematic of the simplified thermal resistance circuit.....	34
Figure 14. Fully assembled frame structure and refrigerated water recirculator	37
Figure 15. Resistive Thermal Device.....	38
Figure 16. Schematic of RTD placement for testing	39
Figure 17. Temperature measures of a typical trial	40
Figure 18. Typical temperature response of recirculating water inside the capillary chamber. ...	41
Figure 19. Graph of theoretical model superimposed on experimental data.	42
Figure 20. Rise time versus convective heat transfer coefficient of air curve.....	45

1.0 Introduction

With the complete mapping of the human genome, researchers have been able to discover the cause of several genetic diseases caused either by a single allele or multiple alleles on a single gene. The understanding of common, but more complex genetic diseases has remained more elusive. Although modern methods which successfully detect genetic variation are available, they are impractical for testing sample populations large enough (10^6 people) to correlate causes of polygenic disorders with specific groups of mutations. To remedy the current deficiency, this project is developing an Ultra-high Throughput Mutational Spectrometer (UTMS) to process genetic samples on a scale orders of magnitude greater than currently available analyzers. Not only will the UTMS have greater throughput than contemporary machines, it will sequester interesting mutations, and have a separation channel arrangement of samples into a 100 by 100 array to minimize its size. At the projected rate with which the UTMS can process genetic material, researchers can feasibly obtain sufficiently large sample populations to definitively correlate small genetic variations with approximately 100 common diseases in only 2 years.

2.0 Genetic Variation

Accurate DNA replication, transcription, and translation depend on reliable pairing of complementary base pairs. Although errors infrequently occur, the consequences can be severe because they are heritable. These errors may involve a single base pair (point mutation) or a fragment of DNA. Mutation of a single base pair may be a substitution, insertion, or deletion. The problem manifests when the mutated DNA strand is transcribed and translated. Single base pair substitutions can lead to the translation of proteins with incorrect amino acid sequences

(missense) or the premature stop of protein synthesis (nonsense). Frame shift mutations, caused by insertion or deletion of base pairs, lead to the translation of completely unintended proteins. It is the phenotypic expression of genetic errors that cause disease.

Chromosomal mutation involves the alteration of fragments of DNA. DNA can randomly break and rejoin either spontaneously or induced [17]. Rejoining errors include deletion, inversion, duplication, and translocation. The mutations are aptly named: deletion removes fragments of the genetic code; inversion rejoins a fragment in a reversed orientation; duplication, often occurring in conjunction with deletion, inserts two copies, originating from a deleted section of a homologous chromosome, of a fragment into the DNA; and translocation results in the splicing of a DNA fragment into a different chromosome, which may or may not be reciprocal. Chromosomal mutation induces extensive change in genetic material, which undoubtedly results in abnormal phenotypic expression.

2.1 Genetic Analysis

Due to the low frequency of occurrence, fewer than 10^{-7} , point mutations are difficult to detect. Complete gene sequencing is impractical for the application because it is a time intensive process. DNA separation techniques such as denaturant capillary electrophoresis and its variants are more suitable, but require high resolution to detect small genetic variations. Electrophoresis is the migration of charged particles through an electric field [17]. The most basic technique is Denaturing Gradient Gel Electrophoresis (DGGE).

Spatial separation in DGGE is based on different melting points of DNA fragments and the reduced electrophoretic mobility of denatured DNA [9]. DNA separation is combined with high fidelity replication techniques such as the polymerase chain reaction (PCR) to improve the

rate of detection [10]. A batch of replicated fragments, spliced with fluorescent tags, is placed in a polymer gel. When a high voltage electric field is applied to the gel, the negatively charged DNA fragments are drawn toward the positive node.

The polymer gel molecules partially inhibit the migration of DNA fragments. Two factors affect the rate at which these fragments move through the gel. First is the size of the macromolecule; smaller fragments move more rapidly through the polymer matrix. The second factor is the molecular composition of fragments. The two nucleic acid chains which form DNA's double helical structure interact through hydrogen bonds. The strength of these bonds depends on the sequence of the polynucleotide chain. The unstable fragments denature at lower temperatures, causing them to migrate slower than the tightly wound counterparts.

An alternative to denaturing gradient electrophoresis is constant denaturing, which uses a zone of constant temperature and denaturant concentration to achieve spatial separation [8]. In addition, capillaries can be used as a medium instead of slab gel. Capillary electrophoresis (CE) is more suitable to large scale parallel processing. Use of small bore quartz capillaries allows increased voltage input of slab gels, which improves throughput time. The large surface area ratio of capillaries allows efficient heat dissipation under high voltage operation. The greatest advantage of capillaries is their suitability for rapid cleaning and gel loading between trials.

A combination of constant denaturing and capillary electrophoresis yields constant denaturant capillary electrophoresis (CDCE). CDCE results display DNA fragment concentrations over a temporal gradient. This method utilizes CE's potential for massively parallel processing. The use of a constant denaturing as opposed to a temperature gradient process simplifies temperature control over a large array of capillaries.

2.2 Mutational Spectrometry

The high throughput and fine resolution of CDCE enables effective mutation detection without phenotypic screening [14]. This capability holds great potential medical advancements in disease prevention. Cancer is a common pathological condition caused by multiple mutations that lead to metastasis [17]. Current medical technology can only detect cancer after a tumor begins to form. If UTMS were used for medical screening, cancer detection could be feasible in its earliest stages of development.

Mutational spectrometry can also lead to a greater understanding of the human genome. Although it has been mapped, discoveries made on the Human Genome Project are far from a full understanding of individual variations in genetic composition. Current genetic research has been able to accurately identify single allele or single gene mutation caused diseases. The barrier current researchers face is the ability to characterize diseases of polygenic cause. The proposed DNA spectral analyzer, capable of 10,000 simultaneous channels of analysis, will be capable of identifying all genetic variants within that sample population. The ability to sequence and compare DNA from large populations may lead to a thorough understanding of common maladies, such as diabetes and heart disease, on polygenic causes.

3.0 Instrument Concept

The Ultra-high Throughput Mutational Spectrometer (UTMS) combines CDCE and end-on fluorescent detection with a high sensitivity camera. The orientation of end-on detection allows the capillaries to be arranged in a rectangular matrix, which increases the throughput potential over conventional CDCE detection. The main structure of the instrument is a modular container which houses the capillary array and a cross-flow recirculating water bath. The tips of

each capillary protrude out opposite ends of the structure, allowing interface with a polymer gel loader below and the fluorescent excitation array above. Design of such an interface was one of the objectives of this research.

The UTMS uses constant denaturant capillary electrophoresis for DNA separation because this process is capable of mutant detection at a fraction of 10^{-6} [14]. Capillary electrophoresis can separate denatured, or partially melted, DNA fragments differing by only a single base pair [14]. Typically, fluorescence detection with CDCE is achieved via laser excitation. Typically, a 30 mW argon laser beam is filtered through a 488 nm filter and focused into a portion of the capillary where the polymer coating is removed [8]. The normal orientation of the laser to capillaries for a 100 by 100 array however, is ineffective. In the UTMS, end-on fluorescent excitation is achieved with an LED array.

Illumination of the 100 by 100 capillary array is achieved with a water-cooled overhead array of blue light emitting diodes (LED). As shown in Figure 1, light from the array, passes through a diffuser, an excitation filter, and a dichroic beam splitter, and a lenslet array before hitting the capillaries. The LED array is current matched for near uniform intensity. Diffusion ensures an approximately uniform light intensity, improving contrast and resolution of the image. The beam splitter directs light emitted from the array towards a horizontally mounted, high sensitivity camera. The camera is a charge coupled device (CCD).

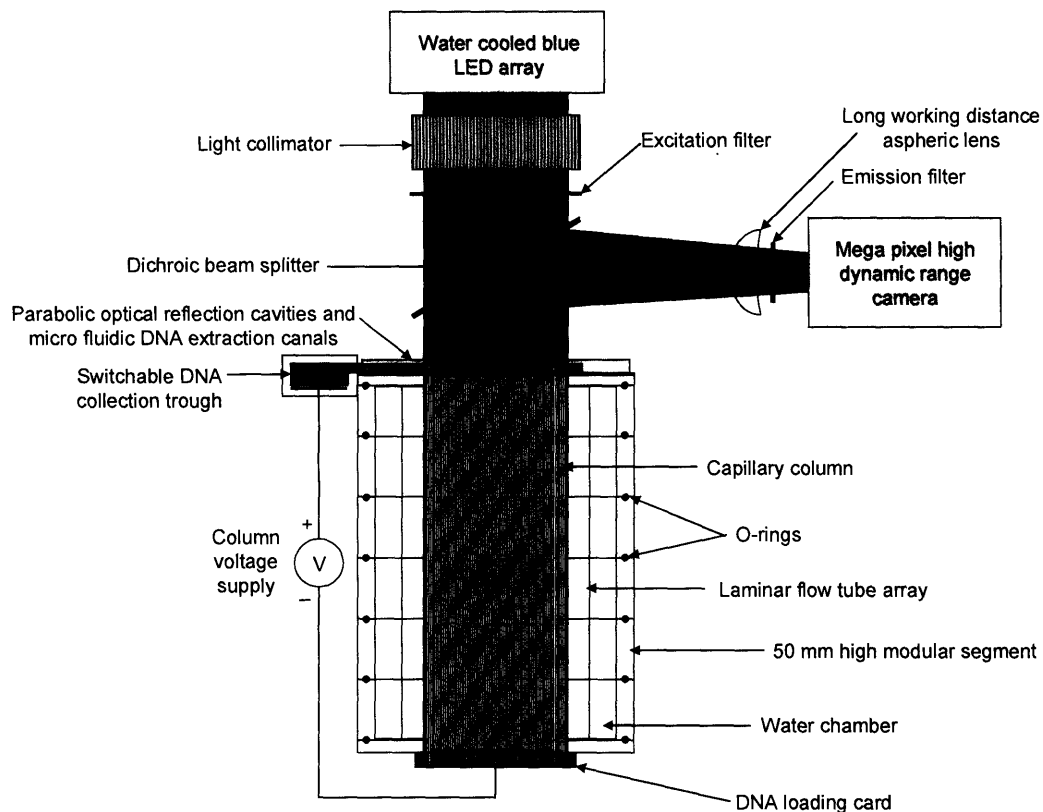


Figure 1. Schematic of ultra high throughput mutational spectrometer (taken from UTMS proposal, Bioinstrumentation Laboratory, MIT).

The main structure of the UTMS is designed to simultaneously constrain the capillary array in parallel and facilitate temperature control during electrophoresis. During experimentation, the temperature variation across the entire 10,000 capillary array must be maintained within ± 0.2 °C precision. Two columns of cross-flow diffusers divide the structure's interior into three chambers; an inlet chamber, the array chamber, and an outlet chamber. The diffusers ensure convective cooling orthogonally across the capillary array. To maximize the surface area to volume ratio, facilitating heat dissipation, the polyamide coated quartz capillaries shown in Figure 2 have a 350 μm outer diameter and 75 μm inner diameter.



Figure 2. Polyamide coated quartz capillary, 350 μm OD, 75 μm ID.

3.1 Design Requirement for Experimental Simulation

The main structure of the UTMS is being developed simultaneously with the CDCE apparatus. The design and manufacture of a modular frame has been completed, but the experimental procedures are not yet functional. The main structure, therefore, must be modified to accept a resistive heating element which can simulate the power input caused by Joule heating in the capillaries during electrophoresis. The simulated heat source must be close to 300 mm long and capable of generating 200 to 275 W power to be dimensionally and functionally similar to the capillary array.

Modifications to the end plates of the modular frame must be made to accept the heat source. Because the current frame will be used in the fully assembled prototype, installation

features must be either universal or scalable with the capillary clamps which constrain the array during experimentation. The bottom plate must be redesigned to interface with gel loading mechanism. The top plate must have a window which exposes the capillary tips to fluorescent detection above, while maintaining a proper seal against the recirculating coolant. Said modifications eliminate the need for further design alterations between simulated and experimental testing.

In addition to newly designed components, the existing modular frame must be improved to eliminate leakage problems. The current design uses O-rings to seal the mating faces of individual frame components. Variables that must be investigated include the flatness of the faces, surface roughness, and O-ring gland geometry. Due to the large surface area of the mating faces, other static seals will also be considered.

4.0 Modifications of the Modular Structure

The primary objectives of this thesis included the design of mounting features to install a capillary array simulating heat source and debugging the modular frame of leakage problems to enable proper testing. The mounting features are modular in design. Said features are based on the dimensions of a 10 by 10 array being used to develop the capillary loading and clamping devices, as well as the gel loader. The clamping plate on which all modifications are based is shown in Figure 3. The design is scalable and does not inhibit the structure's ability to accept a full 10,000 capillary array. All modifications are based on the original CAD models of the main structure.

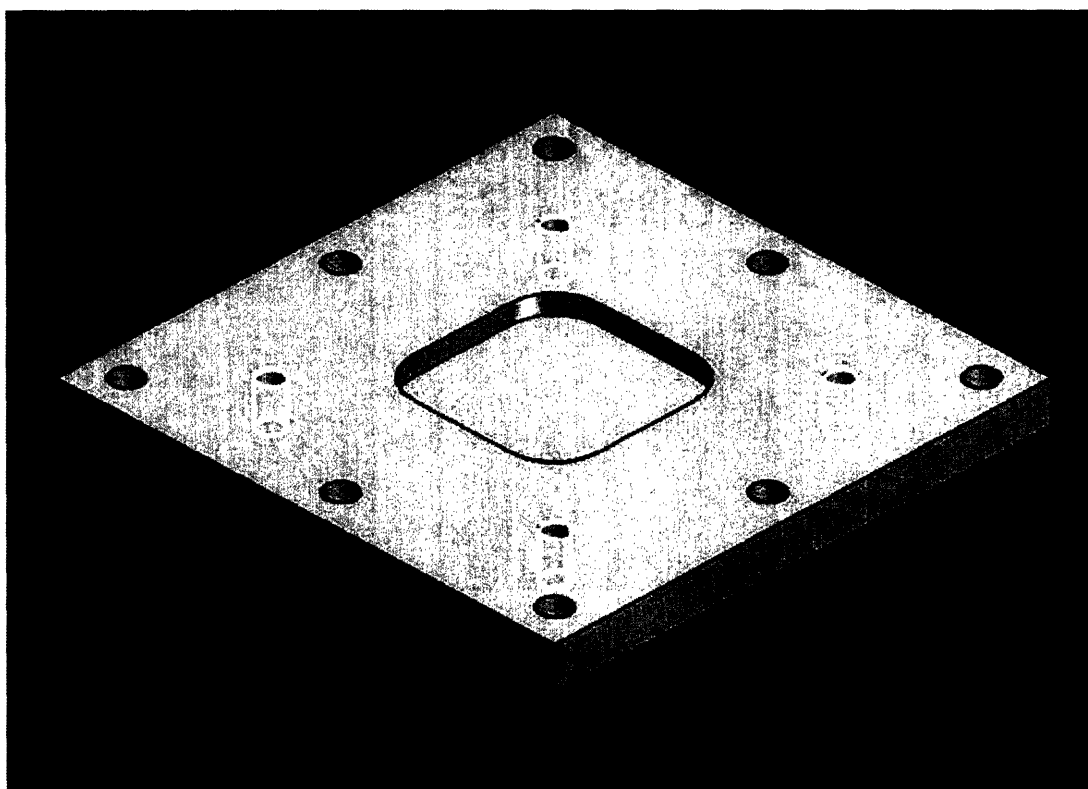


Figure 3. Capillary clamp plate. The 40 by 40 mm 4-bolt pattern is highlighted in yellow.

4.1 End Plate Designs

The top and bottom plates, shown in Figures 4 and 5 respectively, feature similarly dimensioned features which allow the 10 by 10 capillary test array to be installed from the bottom of the fully assembled main structure. The circular cutouts, measuring 30 mm in diameter, fit around the 20 mm square capillary array with sufficient clearance while allowing an O-ring to fit within the 4-bolt pattern, spaced on a 40 mm square. The square pockets measure 51 by 51 mm, aiding the alignment of the 50 mm square capillary clamps.

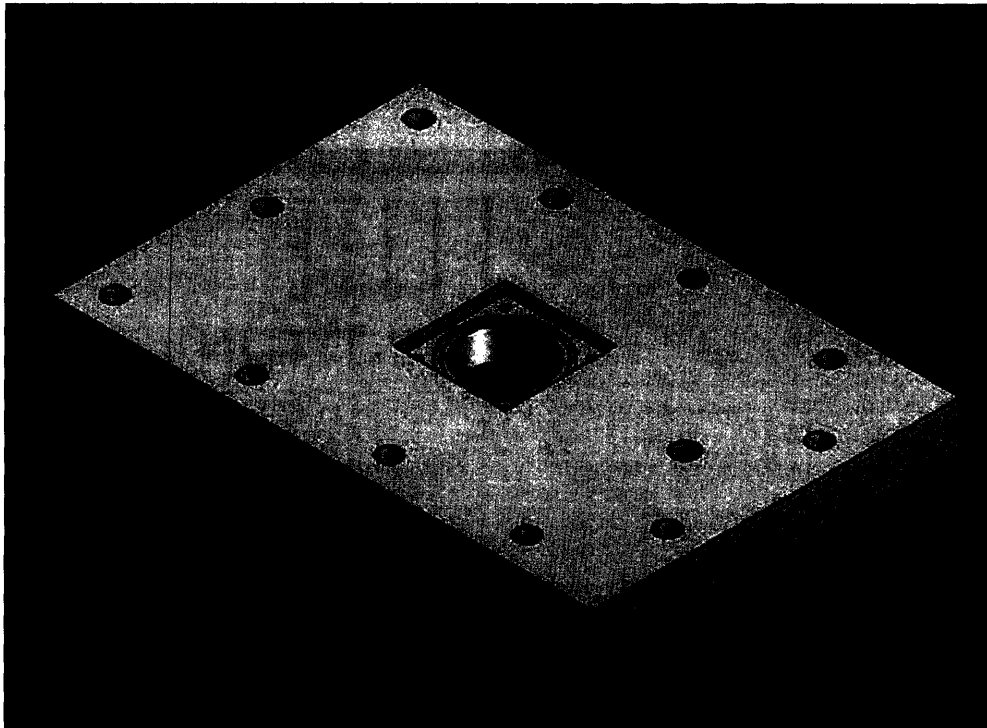


Figure 4. Top plate with square pocket flange adaptor and O-ring gland.

The bottom plate has 6 mm wide rectangular key slots position the main structure's four supports. The supports are made from a modular aluminum framing system (mk Profile Series 25 [13]). Keyed angles, shown in Figure 6 used to mount the supports align within the bottom plate slots and aluminum framing T-slots. The key slots are placed at 45 degree angles to place

the mounting points clear of existing bolt holes. The supports measure 130 mm in length to provide clearance for the gel loader, positioned under the structure.

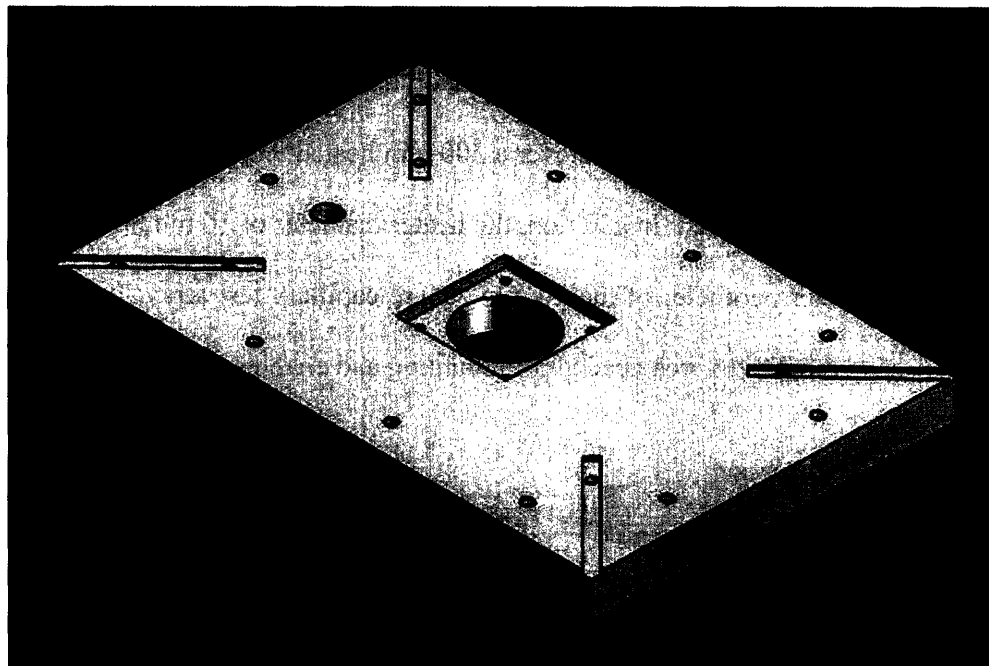


Figure 5. Bottom plate with flange adaptor and 6 mm key slots for mounting supports.



Figure 6. mk Series 25 angle CAD model (left) and mk angle installed in UTMS base (right) (CAD model taken from mk Automation, Inc. [13]).

4.2 Simulated Power Input

The source of simulated capillary array heating, shown in Figure 7, is an immersion type resistive heating element (Omega RI Series [15]). This specific heater was selected because its geometry and performance capability are a close match to those of the 100 capillary test array. Power output can reach upwards of 750 W over a 300 mm heated length. The length is a perfect match for the design requirements. In addition, the heater diameter of 16 mm locates the heating surface close to the outer perimeter of the 20 mm square capillary test array. Installation via a 1/2" NPT screw plug minimizes area needed for mounting and enables water-tight sealing.



Figure 7. Omega RI Series screw plug type immersion heater (taken from Omega Engineering, Inc. [15]).

A square flange, shown in Figure 8, supports and aligns the screw plug immersion heater in the modified top plate. The flange measures 50 by 50 mm, matching the dimensions of the capillary clamp shown in Figure 3. The 4-bolt pattern is taken from the clamp design as well. The flange is 10 mm thick, to ensure the vertical alignment of the heater in the 1/2" NPT tapped center hole. Water-tight sealing is achieved via an O-ring installed below, in the top plate. A similarly dimensioned flange, shown in Figure 9 is designed to seal the opening in the bottom plate. The bottom flange features an O-ring gland to facilitate bottom-up installation.

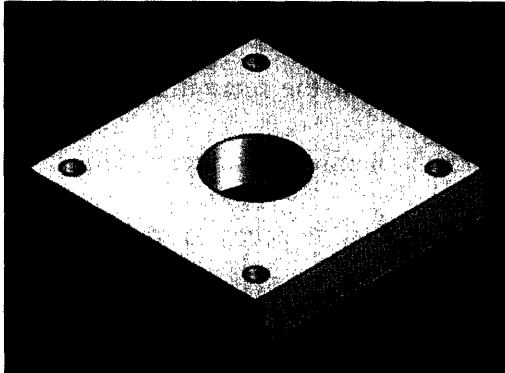


Figure 8. Heater mount flange.

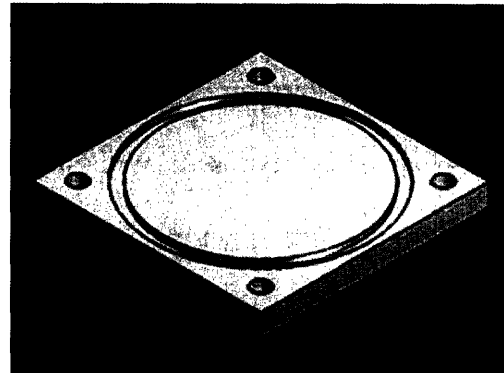


Figure 9. Bottom cap flange.

4.3 Interface with Capillary Array/Gel Loader Assembly

The capillary clamp seen in mounts to 70 by 70 mm plate. The plate is the interface between the clamp and the gel loader. The joint assembly must attach to the bottom of the main structure and provide a water-tight seal around the capillary array. The connector (Figure 10) consists of a square plate welded to a quick clamp tube fitting. The square plate shares the same 4-bolt pattern as the capillary clamp and features an O-ring gland for sealing. An identical connector bolts under the bottom plate of the main structure. A commercial ring gasket sits between the interface of the tube fittings. The clamp (Figure 11) fits over the joint and tightens to provide a seal. The bolts in the clamp are normal to all other interfaces, allowing easy access under the structure.

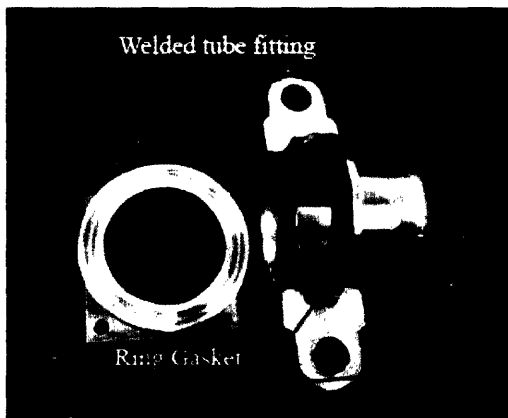


Figure 10. Gel loader-to-main structure connector. The tube fittings seal with a ring gasket.

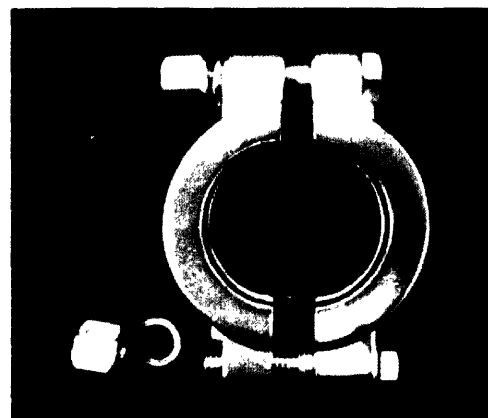


Figure 11. Quick clamp.

4.4 Capillary Array Upper Mount

The capillary array must be constrained at the top of the recirculating chamber with the upper tips exposed. With the capillaries already clamped, a direct interface with the underside of the upper plate would create problems related to access of the bolt heads or alignment. The upper mount (Figure 12) is a 4 mm thick slide that bolts between the uppermost frame piece and the top plate. The structure spanning the width of the chamber provides a mounting surface for the capillary clamp. The clearance holes are countersunk to eliminate interference from bolt heads. The large cutouts allow access under the mount for alignment adjustments.

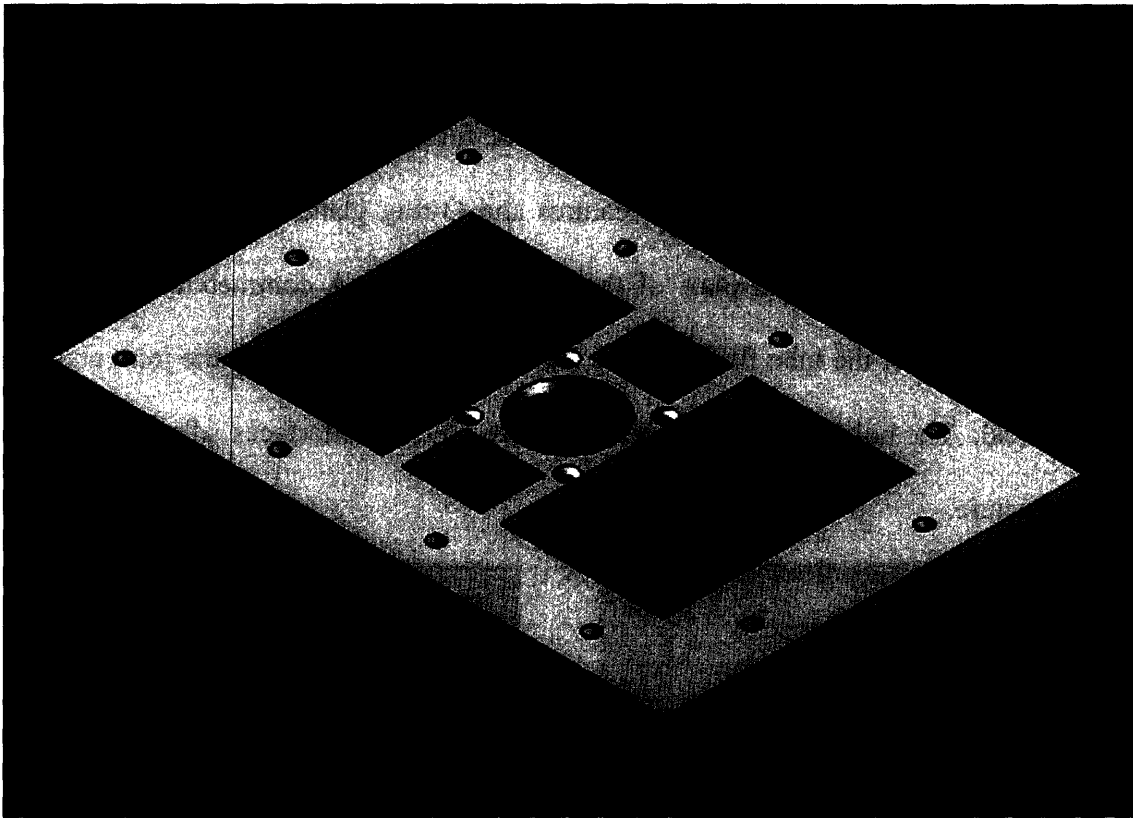


Figure 8. Upper mount plate.

5.0 Manufacturing of Subunit

The predominant cause of leakage in the main structure can be attributed to the modular frame components. Measurement of the flatness of mating surfaces and O-ring gland depths revealed that these dimensions were out of specification. The frame components were surfaced on the Haas VF-OE CNC milling center [4]. O-rings were replaced with flat gaskets, cut on the Trotec laser engraver [20]. The newly designed components were all manufactured on the CNC mill. The modular design of the mounting features and associated flanges allowed the same program to be run on a series of parts before tool change was necessary.

5.1 Modular Frame

Variations in frame thickness were measured using the tool holder on the mill to hold the micrometer and the track for single axis translation. The average discrepancy in thickness was 0.5 mm on an incline. The findings suggest a misalignment of material stock or the vice during initial manufacture. In addition, only one face of each frame component was machined, leaving the opposite as face raw extruded stock. The two mating surfaces of each frame component were refaced with a very fine finish. The depth of cut required to reface the components left the O-ring glands out of specification. The narrow geometry of the gland requires a small diameter endmill to groove. Small tooling requires slow feed rates and would lead to time intensive manufacturing [6].

5.2 Flat Gaskets

An alternative solution to the O-ring design substitutes flat gaskets (Figure 13) for a static seal. Of the gasket materials available, rubber bonded paper was selected for its compatibility as a seal against water. Paper gaskets are one of the thinnest gasket materials available [1]. The fine surface finish on the refaced frame components were suitable for thin gaskets; a combination which allows higher compressive forces and minimizes loss of structural rigidity across the mated surface [1]. The gasket template was created from the CAD model of the modular frame. The 700 mm by 400 mm bed of the Trotec laser engraver could support enough sheet gasket stock to cut 4 gaskets in one run. The simple geometry and thinness of the sheets contributed to low throughput times of under 1 minute per gasket.



Figure 9. Rubber-bonded paper gasket. Manufactured on the Trotec laser engraver (below). Rolled sheet stock pictured above.

5.3 Small Diameter O-Ring Glands

The majority of flanges, connectors, and plugs designed to mount on the end plates featured a gland for 1.6 mm diameter O-rings. These small O-rings provide the seal around the 10 by 10 capillary array. The gland width required is 2.4 mm [11]. For this project, this feature was manufactured using a small diameter endmill. Using conservative feed rates of 30 mm per second traverse, the 30 mm diameter grooves took 45 minutes to machine. Should any of the 50 by 50 mm flanges (Figure 8 and Figure 9) need to be replicated, place the squared stock in a 4-jaw chuck and turn the gland on a lathe.

5.4 Assembly of Subunit

In accordance with the modular frame design, the main structure subunit was assembled from the bottom up, one component at a time. The flat gaskets align on the mating face without interfering with clearance and bolt holes. To ensure a proper seal from the gasket, the bolts were torqued in a cross bolt tightening pattern (Figure 14). Following the pattern, the bolts were hand tightened, torqued until snug, and tightened to full torque. Ideally, gasket performance is optimized when tightening to a specific torque. In this case however, full torque was defined as the limit of hand tightening with a 6mm hex key. The flow diffusers were installed in each modular component without set screws. The inability to accurately align the vertical position of the diffusers could lead to over constraint and exert undue stress on the pieces. Each diffuser was cut 0.5% wider than the frame thickness and compressed when the top plate was installed.

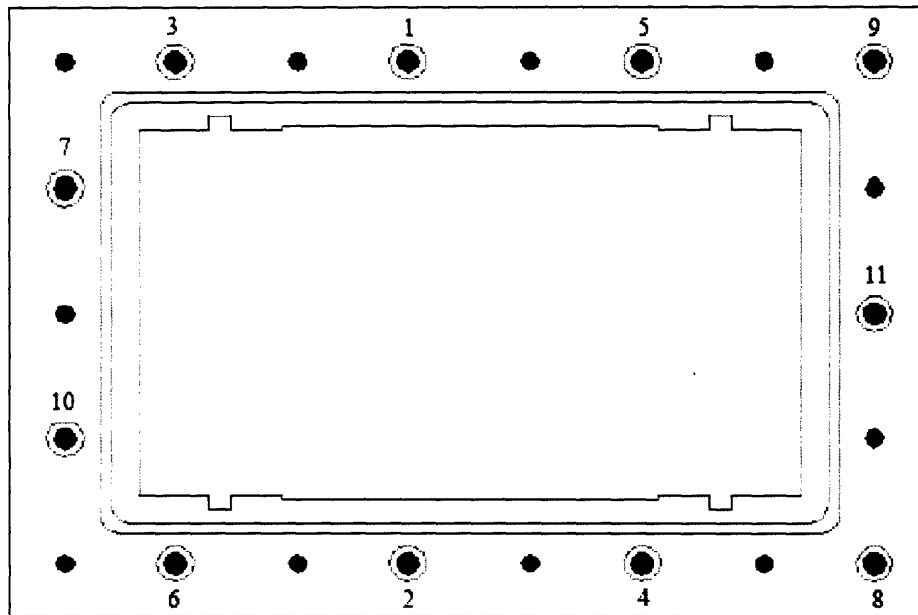


Figure 10. Cross bolt tightening pattern. Tighten in ascending order, loosen in descending.

6.0 Theory

In order to characterize the transient response of the aluminum frame to ohmic resistive heating inside, each element of the system was modeled as a thermal resistance. Heat is transferred into the system by the cylindrical heat source. The thermal circuit consists of conduction and convection from water in cross-flow, conduction through the aluminum frame, and convection off the outer surface of the structure. The convective coefficient of water was derived after characterizing the fluid through the chamber. The governing equation for the system was derived using Newton's law of cooling [5]. The time constant for the system response can be found in that equation.

6.1 Thermal Resistance Model

For a given fluid, the possible modes of heat transfer are conduction, convection and radiation. Due to the atomic structure of solids, only conduction is possible. For the circulating water, radiation will be ruled out because the medium must be transparent to the wavelengths of the energy transfer. The system can be decomposed into a collection of thermal resistances (Figure 15).

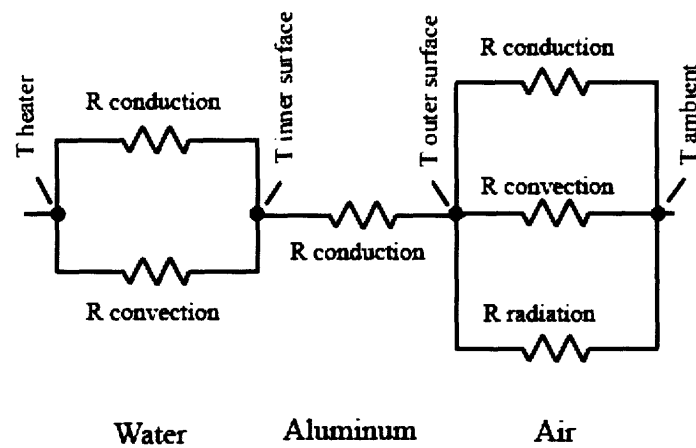


Figure 11. Schematic diagram of thermal resistances.

Conduction is the only mode of heat transfer present in all three media. In steady state, thermal resistance due to conduction, R_{cond} , is a function of distance, area, and thermal conductivity [5].

$$R_{\text{cond}} = \frac{L}{kA}, \quad (1)$$

where L is the length across which conduction occurs, k is the thermal conductivity, and A the area of heat transfer.

Similarly, convection heat transfer is expressed in terms of area and convective heat transfer coefficient such that [5],

$$R_{conv} = \frac{1}{h_c A}, \quad (2)$$

where h_c is the convective heat transfer coefficient, and A is area. For radiation heat transfer [5],

$$R_{rad} = \frac{1}{h_r A}, \quad (3)$$

where h_r is the radiative heat transfer coefficient, and A is area.

The overall thermal resistance of the system is not crucial to modeling the transient response. Calculation of individual resistances can be used to identify dominant processes, and eliminate negligible contributions. Such screening reduces the number of variables when solving Newton's law of cooling.

The thermal resistance model of the current experimental setup is based on a control volume projected normally from the face of the heater (Figure 16). The heating element, although cylindrical, was modeled as a flat surface to better characterize the capillary array. With the given control volume, it is assumed that conduction through aluminum does not result in heat loss through adjacent material outside.

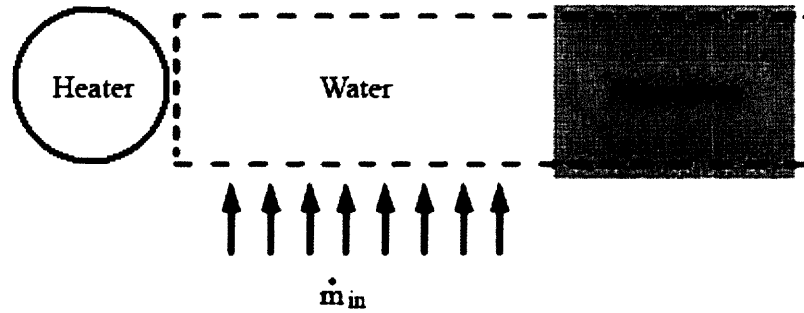


Figure 12. Control volume of frame used for theoretical model. The height of the chamber capillary array chamber, into the page, measures 300 mm.

6.2 Convection Heat Transfer Through Water

Water flow through the capillary chamber is driven by a recirculator. The forced flow over the capillaries must be characterized using the Reynolds number [21]. This dimensionless value will reveal whether the flow is laminar or turbulent. The Reynolds number, Re_D , which is the ratio of inertial forces in the flow to viscous forces along the walls, is expressed as

$$Re_D = \frac{vD_h\rho}{\mu}, \quad (4)$$

where D_h is the hydraulic diameter of the flow, v is the velocity of water through the chamber, and ρ and μ are the density and viscosity of water, respectively. The hydraulic diameter, D_h , is a characteristic dimension of the flow geometry such that

$$D_h = \frac{4A_c}{\wp}, \quad (5)$$

where A_c is the cross sectional area of the chamber and \wp is the wetted perimeter. The velocity of water through the chamber depends of the volumetric flow rate, governed by the recirculator. Exact flow rates for individual pump speed settings are provided by the

manufacturer. Flow velocity can be derived from volumetric flow rate, \dot{V} , using the following relation

$$\dot{V} = A_c v. \quad (6)$$

The flow through the experimental chamber is laminar. Reynolds number used in conjunction with the Prandtl number can be used to derive the Nusselt number, which characterizes temperature gradient. The Prandtl number, Pr, varies based on experimental conditions and must be referenced from a thermal fluid properties chart [3]. In laminar flow, through the temperature range in which the water bath will operate, the Nusselt correlation, Nu_D , for flow across a cylinder is [12]

$$\overline{Nu}_D = 0.3 + \frac{0.62 Re_D^{1/2} Pr^{1/3}}{\left[1 + (0.4 / Pr)^{2/3}\right]^{1/4}}. \quad (7)$$

The correlation in Equation 7 characterizes convection heat transfer across a single cylinder. In the case of the capillary array, which is comprised of multiple banks of cylinders, the Nusselt must be adjusted with an arrangement factor such that

$$\overline{Nu}_D^{10+} = \Phi \overline{Nu}_D^1, \quad (8)$$

where Φ is the arrangement factor and \overline{Nu}_D^1 is the Nusselt number from Equation 7. The 10+ superscript denotes an array of 10 or more cylinders. The full derivation of Φ can be found in Appendix B. The convective heat transfer coefficient can be calculate using

$$h_c = \frac{\overline{Nu}_D}{L_c} k. \quad (9)$$

6.3 Lumped Thermal Capacitance Model

In order to model the transient response in the aluminum frame, the dominant heat transfer mechanism must be identified. In characterizing the thermal response of a solid experiencing heat transfer to a fluid, the Biot number, Bi , can be used to identify the principal resistance. The ratio of internal conduction resistance to external convection resistance is

$$Bi = \frac{h_{c,w}L_c}{k_{Al}}, \quad (10)$$

where $h_{c,w}$ is the convective heat transfer coefficient of the water in cross-flow, L_c is the characteristic length, and k_{Al} is the thermal conductivity of aluminum.

In the case of aluminum, undergoing convection heat transfer from water and air, its high thermal conductivity makes its thermal resistance negligible. The situation is suitable for the lumped thermal capacitance model, which assumes the spatially uniform temperature throughout the solid.

6.4 Deriving the Transient Model

An examination of the parallel resistances (Figure 15), allows an elimination of elements that do not promote heat transfer. On the outer surface of the aluminum frame, heat transfer through air is dominated by convection. Air is a poor thermal conductor and therefore resists conductive heat transfer. The anodized finish on the aluminum does improve the emissivity, but radiation is a poor form of heat transfer. Conversely, the thermal resistance of the aluminum is too small to induce a temperature gradient, as revealed in Section 6.4, rendering its contribution negligible. The individual thermal resistances are calculated in Appendix C. The thermal circuit is reduced to three

elements: conduction and convection through the recirculating water on the inner face and natural convection in air on the outer surface (Figure 17).

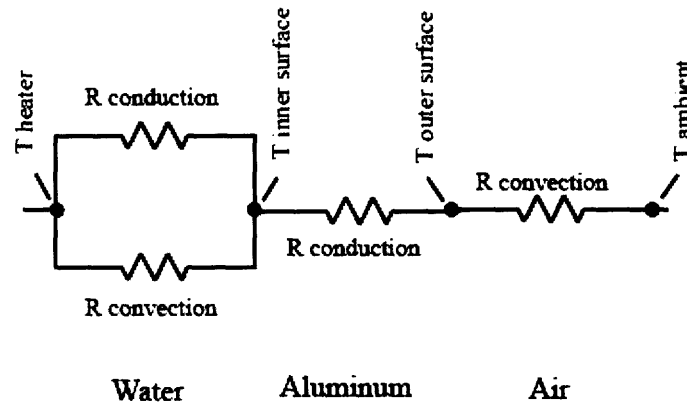


Figure 13. Schematic of the simplified thermal resistance circuit.

The transient model can be derived by combining the Fourier Conduction Law and the first law of thermodynamics [5]. Fourier's law expresses energy flow rate as a function of spatial temperature gradient. In the case where the path of conduction is known, heat transfer, \dot{Q} , can be expressed in the integrated form,

$$\dot{Q} = \frac{-kA}{L}(T_1 - T_2), \quad (11)$$

where k is the thermal conductivity, A is the area of heat transfer, and L is the length over which conduction occurs. In this model, T_1 is the temperature of the heater and T_2 is the temperature at the outer surface of the aluminum. The form of Equation 11 should be recognizable as a function of thermal resistance, such that

$$\dot{Q} = \frac{1}{R_{th}}(T_1 - T_2). \quad (12)$$

In this form, Fourier's law can be applied to all three modes of heat transfer. Equation 12 assumes that heat transfer into the system has reached steady state.

The differential form of the first law of thermodynamics is expressed in terms of a temporal temperature gradient,

$$\dot{Q} = \rho cV \frac{dT}{dt}, \quad (13)$$

where ρ is the density, c is the thermal capacitance, and V is the volume of aluminum in the control volume. Combining Equation 13 with Equation 12, applied to the three heat transfer elements, yields

$$(\rho cV)_{Al} \frac{dT_{Al}}{dt} = \left[\frac{k_w A_h}{L} (T_{heater} - T_{Al}) + h_{c,w} A_h (T_w - T_{Al}) \right] - h_{c,a} A_h (T_{Al} - T_a). \quad (14)$$

Expanding and rearranging Equation 14 into the form

$$dT_{Al} = \left[T_{Al} \frac{A_h \left(-\frac{k_w}{L} - h_{c,w} - h_{c,a} \right)}{\rho cV} + \frac{A_h \left(\frac{k_w}{L} T_{heater} + h_{c,w} T_w + h_{c,a} T_a \right)}{\rho cV} \right] dt, \quad (15)$$

allows it to be integrated. Equation 15 is arranged such that all the time-invariant parameters are grouped together. To facilitate integration, these parameters can be consolidated into two constants,

$$A = \frac{A_h \left(-\frac{k_w}{L} - h_{c,w} - h_{c,a} \right)}{\rho cV}, \quad B = \frac{A_h \left(\frac{k_w}{L} T_{heater} + h_{c,w} T_w + h_{c,a} T_a \right)}{\rho cV}. \quad (16)$$

Equation 15 simplifies to

$$dT_{Al} = (T_{Al} A + B) dt, \quad (17)$$

which reduces the differential equation to three terms, making it easier to solve. Single integration over time, t , yields

$$T_{Al} = Ce^{At} - \frac{B}{A}, \quad (18)$$

where C is the constant of integration. The constant can be solved by applying boundary conditions. At time $t = 0$, $T_{Al} = T_i$, where T_i is the initial steady-state temperature of the aluminum frame. Substituting C back into Equation 18 yields

$$T_{Al} = \left(T_i + \frac{B}{A} \right) e^{At} - \frac{B}{A}, \quad (19)$$

with a time constant of

$$\tau = -\frac{1}{A} = \frac{\rho c V}{A_h \left(\frac{k_w}{L} + h_{c,w} + h_{c,a} \right)}. \quad (20)$$

The transient model of the aluminum frame response to heating within the chamber is a first order system. The positive time constant, τ , indicates that the system's response will exhibit exponential decay.

7.0 Simulated Testing of the Thermal Response

The modular aluminum structure houses the capillary array and the recirculating water bath used for temperature control (Figure 18). Each capillary behaves like a resistive heating element, jointly transferring approximately 275 W into the chamber. The water used to cool the array is maintained at temperatures well above ambient, in the operating temperature domain of CDCE. For testing purposes, the energy flow rate into the system will be simulated by an immersion type resistive heating element. The large volume, refrigerated recirculator (PolyScience Model 9601) provides heating and cooling as necessary for temperature control.

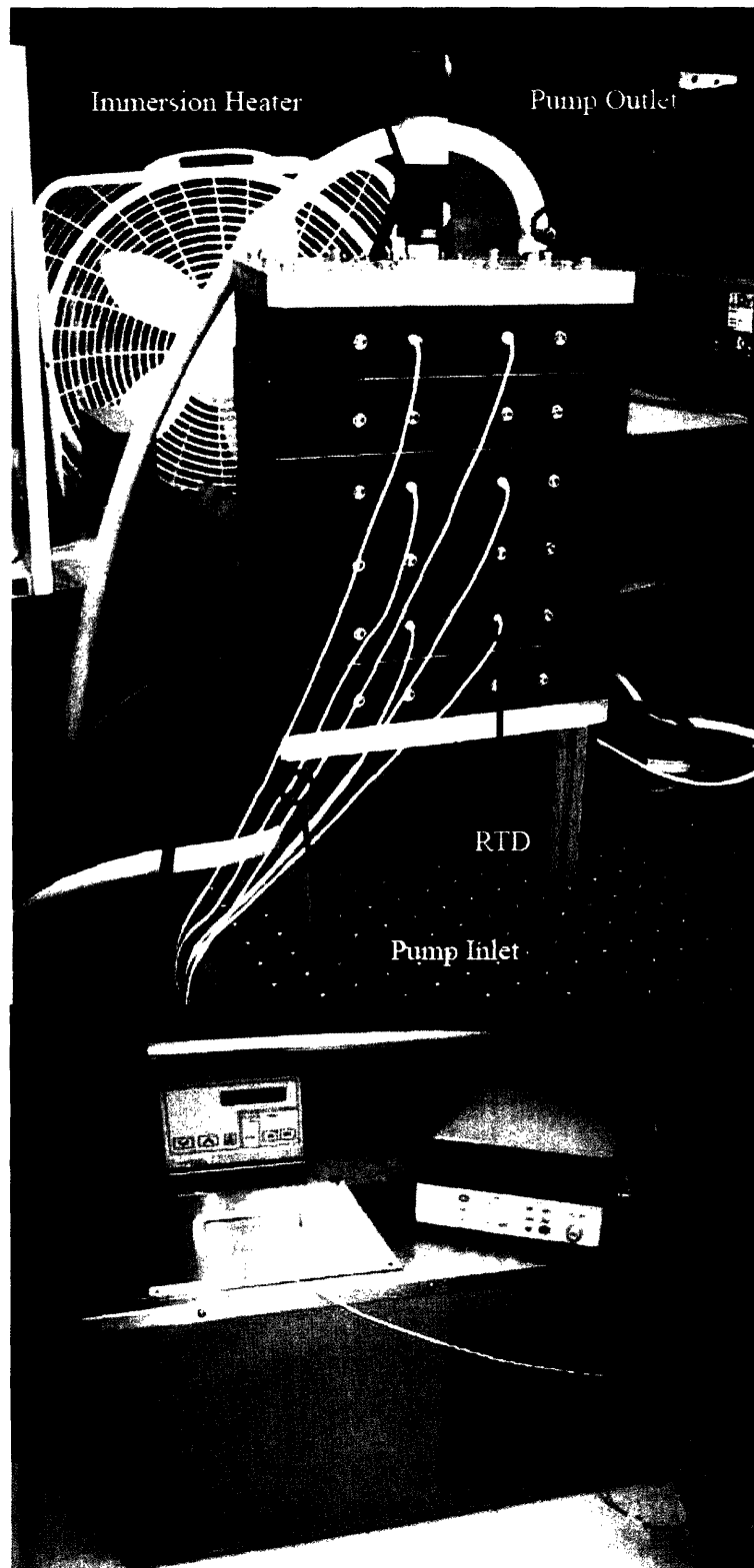


Figure 14. Fully assembled frame structure with recirculator plumbing connected and RTDs installed (top). Refrigerated water recirculator (bottom).

When the resistive heating element is powered, a simultaneous transient response in the heater, water, and aluminum frame will occur. A detailed analysis of the thermal response in water is presented by Suen [19]. The focus of this research is to characterize the response in the aluminum frame and verify the model. Temperature data are gathered on the circulating water and the outer surface of the aluminum.

7.1 Procedure

Thermal measurements were taken with resistive thermal devices (RTD) shown in Figure 19. Seven individual sensors, connected to a data acquisition system, were mounted to the system. Three were installed in the modular frame, downstream of the heater, along the height of the structure. These would measure the outlet temperature of the circulating water. Three more were taped to the outer surface of the frame at similar heights, to verify the theoretical model (Figure 20). The final RTD was placed in the recirculator reservoir to monitor inlet temperature.



Figure 15. Resistive Thermal Device. Teflon tape is wrapped around the wire for water tight installation.

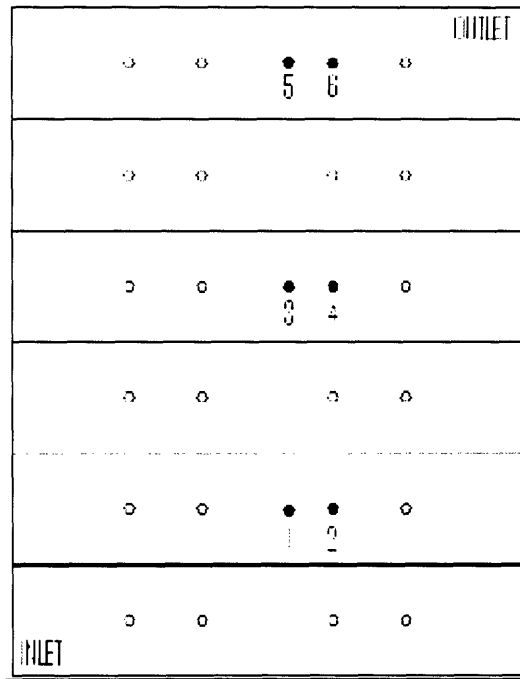


Figure 16. Schematic of RTD placement for testing. Red demarks sensors installed inside the chamber. Blue demarks sensors installed on the outer surface of the frame.

The heating element was connected to a DC power supply. The resistance across the heater was measured to determine voltage and current input. The tests were run applying 250 W input from the heater. Data logging was started once the heater was turned on. Between successive trials, the recirculator was allowed to run with the heater off until the system reached initial steady state conditions.

8.0 Results

Temperature data gathered from the test runs was able to verify the theoretical model and shed qualitative insight on the thermal properties of the system. Figure 21 shows a typical trial run. The concentration of three inputs at the top of the graph, the even channels, represents water temperature readings within the capillary chamber. The

flat line below it is the recirculator reservoir temperature. The remaining channels show the surface temperatures of the aluminum frame. Channel 1, the bottom-most line represented in blue, was placed nearest the base. Channel 5 was located nearest the top of the structure.

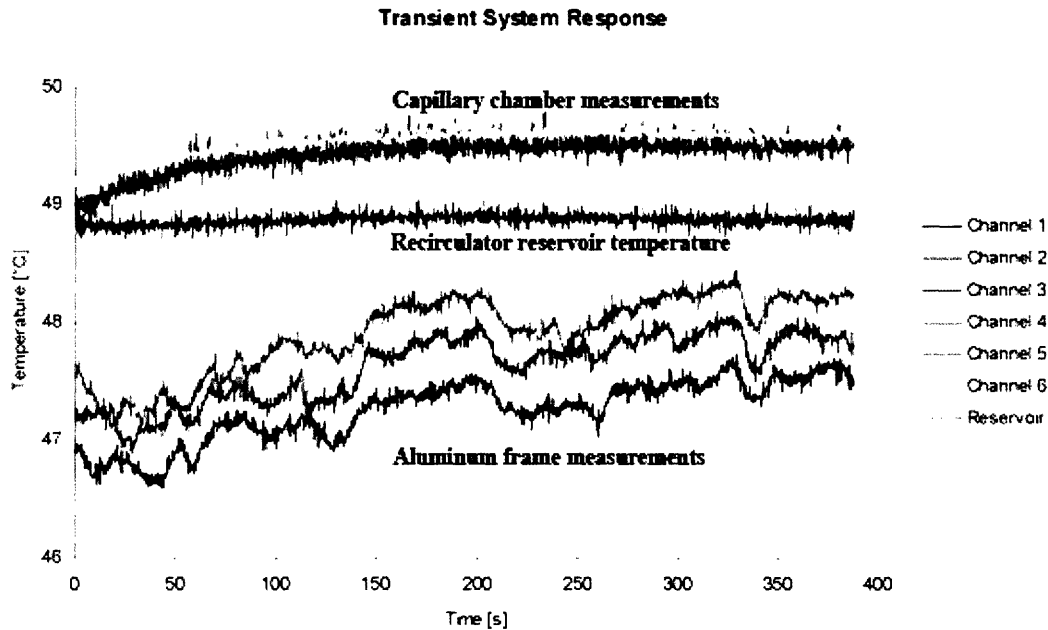


Figure 17. Temperature measures of a typical trial. The capillary chamber temperature is uniform along the frame height. The frame itself however, exhibits a temperature gradient.

Observation of the recirculating water's response to thermal input will reveal that the capillary chamber temperature is relatively inert to the heat transfer. Figure 22 shows the averaged temperature reading of all three RTDs placed in the recirculating water. The experimental trials were performed under the assumption that the recirculator's set temperature (48.9 °C) would be the desired steady state. The steady-state temperature of the capillary chamber was 49.5 °C. This shows a 0.6 °C steady-state error. The 90% rise time in the chamber was approximately 125 seconds. During the circulating water

heating transient, the reservoir temperature only increased by 0.08 °C and resettled to the initial steady state temperature in approximately 2 minutes. This suggests that the recirculator will be the primary agent of temperature control.

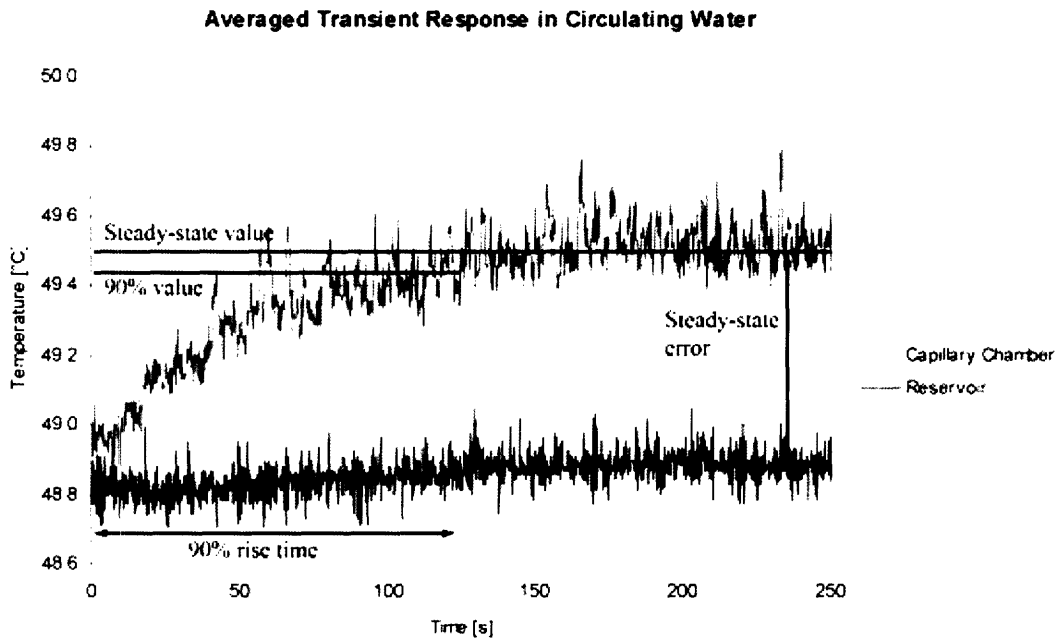


Figure 18. Typical temperature response of recirculating water inside the capillary chamber.

A graph was generated from the theoretical model, using the initial conditions of the trial at inputs. Figure 23 shows the theoretically generated curve was superimposed on the temperature data. The system's time constant is accurately characterized by the model. The experimental data feature an unsteady temperature reading on the aluminum's surface. This is possibly caused by noise from the ambient environment. Unlike the RTDs in the chamber, the ones on the surface are not immersed in the medium being measured. Mounted to the frame using insulated tape, one side of the RTD is not

in contact with the aluminum at all. Although insulated, the tape could not provide a secure seal around the RTD, allowing convective cooling from ambient air.

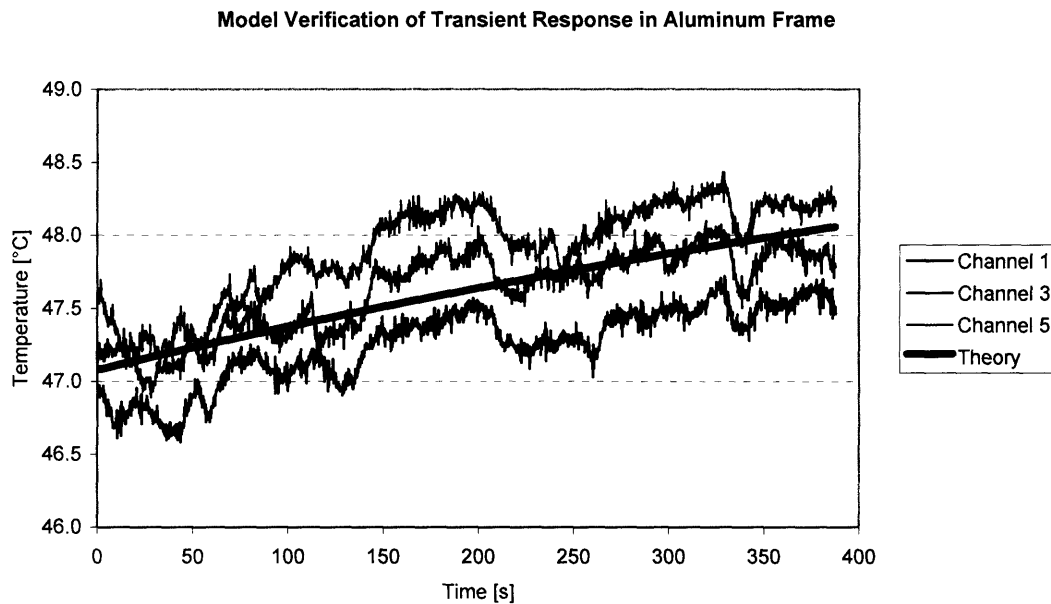


Figure 19. The curve generated from the theoretical model superimposed on experimental data.

Correlating the temperature curves from each channel to their relative location on the structure reveals a temperature gradient in the vertical direction. Channel 5 near the top of the frame recorded the highest temperatures, while channel 1 nearest the base recorded the lowest. The cause of the gradient was originally attributed to poor heater performance. It was assumed that the heater may not heat along its entire length. Temperature measurements recorded along the length of the heater proved otherwise. The actual cause of the problem is attributed to poor insulation between the heating element and the fitting. The NPT fitting on the heater is made of brass, which has a high thermal conductivity, was transferring heat to the aluminum plate it mounted in. Without

the convective cooling of the circulating water, temperature differences of up to 13 °C can exist between the upper- and lower-most RTDs.

9.0 Conclusion and Outlook

The main structure of the UTMS has been debugged of leakage problems. While the primary design of the subunit remains unchanged, modifications were made to the end plates to allow interface with other components of the instrument. The modifications are completely modular in design, allowing the installation of various components on the subunit as long as standard 50 by 50 mm square flanges are used for mounting. The subunit has already been used in successive data gathering experiments, which proves the functionality of its current design.

With the completion of this iteration of the subunit prototype, future design considerations should be made for continued development. The current frame is large and heavy. If cooling of the capillary chamber is a concern for the UTMS, then a reduction in mass will decrease the time constant (see Equation 20). A reduction in the surface area of the mating faces will also make the frame more suitable to the use of O-rings. Further development of the frame should incorporate design for manufacturing (DFM). DFM should not only pertain to improving throughput time of machining, but to assembly as well. The current modular design guarantees a good seal and even load distribution across the mating faces, but requires approximately 1.5 minute per frame component in assembly time.

In its current state, the capillary chamber subunit is capable of operation with the 10 by 10 test array. Installation strategies for the clamped array have been considered.

The only foreseeable obstacle is alignment through the capillary slides, which are intended to provide structural support along the 300 mm length of the capillaries. The current interfaces have been tested with the installation of an immersion type resistive heater. The strategy is scaleable for the full 100 by 100 capillary array, by enlarging the mounting features. The interface with a capillary clamp, mounted in the gel loading mechanism, remains to be tested. If the interface is functional, the product of this research will enable the first trials of the UTMS system functioning together.

The experimental data and theoretical model can be used to determine the design requirements of a fully operational system. For operation within the experimental temperature domain, the settling time of the capillary chamber temperature was in the vicinity of 2 minutes. During the transient, temperature within the chamber will not be within ± 0.2 °C precision specified by the instrument design requirements. A possible solution to this problem is the incorporation of a lead in domain, which allows the temperature to settle before the DNA samples reach the test chamber. Proper characterization of the settling time and its correlation with temperature conditions will be necessary to define the lead length.

The 2 minute settling time also suggests that the system's thermal response to Joule heating is relatively inert. Material selection and design of the frame structure can influence this property. The time constant of the frame's transient response is directly proportional to its mass and thermal capacitance, and inversely proportional to the convective heat transfer coefficient of air on the outside surface. While the time constant is also inversely proportional to thermal properties of the recirculating water flow, the current instrument concept is designed to use water as a coolant. Figure 24 shows the

correlation between the time constant of the aluminum frame transient response and convective heat transfer coefficient of air.

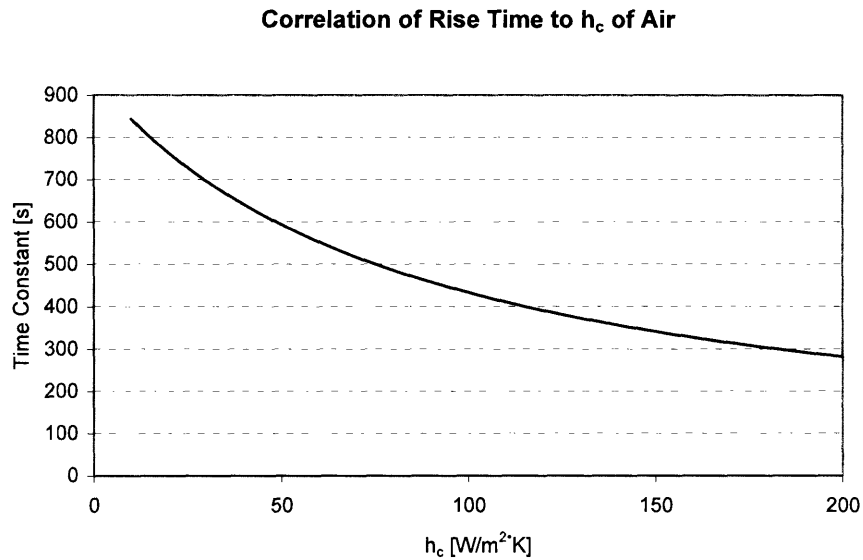


Figure 20. Rise time versus convective heat transfer coefficient of air curve. This graph shows the effect of introducing forced convection across the outer surface of the chamber for typical forced convection h_c values.

Over the typical range of convective heat transfer coefficient values for forced convection in air (10 to 200 W/m²·K [12]), the time constant of the aluminum frame transient can be reduced by 66.7%. A combination of cooling from the recirculator and heat dissipation from the frame can result in faster temperature control system. A reduced time constant will allow for finer control of the system response, but will make the system more susceptible to ambient noise. The transient time constant will need be optimized to match the capabilities of the recirculator to decrease the overall system response time.

Furthermore, characterization of the steady-state error will be important for the design of the temperature control scheme. The assumption made during experimentation,

that the steady-state temperature could be defined as the recirculator set temperature, is incorrect. Trials performed in the 50 °C temperature range revealed an error of 0.6 °C. Correlating the steady-state error to the recirculator set temperature will allow proper calibration of the set temperature.

References

1. Brown, M. *Seals and Sealing Handbook*. Oxford; Publisher's Limited, 1990.
2. Crane, B., Hogan, C., Lerman, L. and Hunter, I.W. DNA mutation detection via fluorescence imaging in a spatial thermal gradient, capillary electrophoresis system. *Review of Scientific Instruments*, 72(11): 4245-4251, 2001 Nov.
3. Cravalho, E., Smith, J. Jr, Brisson, J., McKinley, G. *Thermal Fluids Property Data*. Cambridge: Oxford University Press, 2002.
4. Haas Automation, Inc, Oxnard, California. <http://www.haascnc.com>.
5. Incropera, F. and DeWitt, D. *Fundamentals of Heat and Mass Transfer*. New York: Wiley, 2001.
6. Kalpakjian, S. *Manufacturing Engineering and Technology*. New York: Addison-Wesley, 1995.
7. Khrapko, K., Coller, H., Andre, P., Li, X.C., Foret, F. and Karger, B.L. and Thilly, W.G. Mutational Spectrometry without phenotypic selection: human mitochondrial DNA. *Nucleic Acids Research*, 25(4): 685-693, 1995.
8. Khrapko, K., Hanekamp, J.S., Thilly, W.G., Belenkii, A., Foret, F. and Karger, B.L. Constant denaturant capillary electrophoresis (CDCE): a high resolution approach to mutational analysis. *Nucleic Acids Research*, 22(3): 364-369, 1994.
9. Lerman, L.S. and Frisch, H.L. Why does the electrophoretic mobility of DNA in gels vary with the length of the molecule? *Biopolymers*, 21(5): 995-997, 1982.
10. Li, X.C., Khrapko, K., Andre, P.C., Marcelino, L.A., Karger, B.L. and Thilly, W.G. Applications of constant denaturant capillary electrophoresis/high-fidelity polymerase chain reaction to human genetic analysis. *Electrophoresis*, 20(6): 1224-1232, 1999.
11. *Machinery's Handbook 26*. Opamp Technical Books: Los Angeles, 2003
12. Mills, A.F. *Basic Heat and Mass Transfer*. Prentice Hall, 1998.
13. mk Automation, Inc., Bloomfield, Connecticut. <http://www.mkprofiles.com>.
14. Muniappan, B.P. and Thilly, W.G. Application of constant denaturant electrophoresis (CDCE) to mutation detection in humans. *Genetic Analysis*, 14(5-6): 221-227, 1999.
15. Omega Engineering, Stamford, Connecticut. <http://www.omega.com>.

16. PolyScience, Division of Preston Industries, Inc., Niles, Illinois.
<http://www.polyscience.com>.
17. Purves, W.K., Sadava, D., Orians, G.H., Heller, H.C. *Life*. Sinaue Associates, 2001.
18. Slocum, A. *Precision Machine Design*. Michigan: Society of Manufacturing Engineers, 1992.
19. Suen, T. Temperature Response of the Ultra-high Throughput Mutational Spectrometer. BS Thesis, Massachusetts Institute of Technology, Cambridge, MA. 2005.
20. Trotec Laser, Inc., Jackson, Missouri. <http://www.trotec.net>.
21. White, F.M. *Fluid Mechanics*, Boston: McGraw Hill, 1999.

Appendix A: Determination of h_c for Recirculating Water

The Reynolds number was derived from the volumetric flow rate of the recirculator provided by the manufacturer (Polyscience). For the experimental conditions with the pump running at full speed, $\dot{V} = 20$ L/min

$$\dot{V} = 20 \frac{L}{\text{min}} \cdot \frac{1m^3}{1000L} \cdot \frac{1\text{min}}{60s} = 3.33 \times 10^{-4} m^3 / s$$

The cross sectional area of the chamber measured 104 mm in width and 300 mm in height.

$$v = \frac{\dot{V}}{A_c} = \frac{3.33 \times 10^{-4} m^3 / s}{(0.104m)(0.300m)} = 0.0107 m / s$$

Using the thermal-fluid properties of liquid water at 50 °C and atmospheric pressure [3],

$$\begin{aligned}\rho &= 988.03 \text{ kg/m}^3 \\ \mu &= 5.4685 \times 10^{-4} \text{ kg/m}\cdot\text{s} \\ k &= 0.64359 \text{ W/m}\cdot\text{K} \\ \text{Pr} &= 3.5528\end{aligned}$$

$$\text{Re}_D = \frac{(0.0107m/s)(0.154m)(988.03kg/m^3)}{(5.4685 \times 10^{-4} kg/m \cdot s)} = 2.98 \times 10^3$$

Given that $\text{Re}_D < 10^4$ and $\text{Pr} > 0.5$, the Nusselt correlation for a single cylinder becomes,

$$\overline{Nu}_D = 0.3 + \frac{0.62 \text{Re}_D^{1/2} \text{Pr}^{1/3}}{\left[1 + (0.4/\text{Pr})^{2/3}\right]^{1/4}} = 0.3 + \frac{0.62(2980)^{1/2} (3.5528)^{1/3}}{\left[1 + (0.4/3.5528)^{2/3}\right]^{1/4}} = 11.32$$

$$h_c = \frac{\overline{Nu}_D}{L_c} k = \frac{11.32}{(0.104m)} (0.64359 \text{ W/m}\cdot\text{K}) = 70.1 \text{ W/m}^2 \cdot \text{K}$$

Appendix B: Nusselt Number Arrangement Factor

For an array of cylinders, the Nusselt number is modified by a factor Φ , such that

$$\Phi_{aligned} = 1 + \frac{0.7}{\Psi^{1.5}} \cdot \frac{(S_L/S_T - 0.3)}{(S_L/S_T + 0.7)^2}$$

where S_L is the transverse pitch and S_T is the longitudinal pitch. Dimensionless transverse and longitudinal pitches can be described at $P_L = S_L/D$ and $P_T = S_T/D$ respectively, where D is the cylinder diameter. Ψ is defined as

$$\Psi = 1 - \frac{\pi}{4P_T} \quad \text{for } P_L \geq 1.$$

In the case of the capillary array, $S_L = S_T = 1$ mm and $D = 350$ μm , so $P_L = 2.86$. $\Phi_{aligned}$ becomes

$$\Phi_{aligned} = 1 + \frac{0.7}{(0.725)^{1.5}} \cdot \frac{(1-0.3)}{(1+0.7)^2} = 1.275$$

The corrected Nusselt number is

$$\overline{Nu}_D^{10+} = \Phi \overline{Nu}_D^1 = (1.275)(11.32) = 14.43.$$

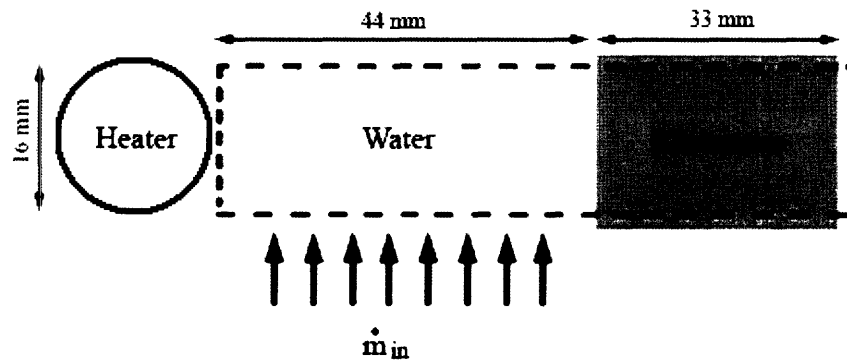
Appendix C: Thermal Resistance Calculations for the Subunit Thermal Circuit

The following are calculations for individual resistances shown in the complete thermal resistance diagram shown in figure 15. Table 1 lists the thermal-fluid properties of water, aluminum, and air that will be used in the calculations.

Table 1. Thermal-Fluid Properties of System Materials. [3]

Conductivity of Water	0.64359 W/m·K
Conductivity of Aluminum	236.8 W/m·K
Conductivity of Air	0.02644 W/m·K
h_c of recirculating water flow	70.1 W/m ² ·K
h_c of natural convection in air	10 W/m ² ·K
Emissivity of Aluminum	0.87

Using the following control volume, the area used in the calculations will be the 16 by 300 mm cross sectional area of the heat transfer.



The thermal resistances are calculated using

$$R_{cond} = \frac{L}{kA}, \quad R_{conv} = \frac{1}{h_c A}, \quad R_{rad} = \frac{1}{\epsilon \sigma A}$$

where L is 33 mm, and σ is the Stefan Boltzmann constant ($5.67 \times 10^{-8} \text{ W/m}^2 \text{ K}^4$). Table 2 lists each of the thermal resistances involved in the thermal circuit.

Table 2. Thermal Resistances of theoretical thermal circuit.

Resistance	Value [K/W]
Conductive in water	2.974
Convective in water	14.243
Conductive in aluminum	0.0337
Conductive in air	366.7
Convective in air	20.83
Radiative in air	1.54×10^9

Table 2 shows that in air, heat transfer is dominated by convection. Conductive and radiative resistances are too large to promote heat transfer. The resistance of aluminum is negligible.